

Parametric instability in the pure-quartic nonlinear Schrödinger equation

Yun-Hong Zhang(张云红) and Chong Liu(刘冲)

Citation: Chin. Phys. B, 2024, 33 (**3**): 030506. DOI: 10.1088/1674-1056/ad11e7
Journal homepage: http://cpb.iphy.ac.cn; http://iopscience.iop.org/cpb

What follows is a list of articles you may be interested in

Dual-wavelength pumped latticed Fermi-Pasta-Ulam recurrences in nonlinear Schrödinger equation

Qian Zhang(张倩), Xiankun Yao(姚献坤), and Heng Dong(董恒)
Chin. Phys. B, 2024, 33 (**3**): 030502. DOI: 10.1088/1674-1056/ad181e

Modulational instability of a resonantly polariton condensate in discrete lattices

Wei Qi(漆伟), Xiao-Gang Guo(郭晓刚), Liang-Wei Dong(董亮伟), and Xiao-Fei Zhang(张晓斐)
Chin. Phys. B, 2023, 32 (**3**): 030502. DOI: 10.1088/1674-1056/ac891a

Formation mechanism of asymmetric breather and rogue waves in pair-transition-coupled nonlinear Schrödinger equations

Zai-Dong Li(李再东), Yang-yang Wang(王洋洋), Peng-Bin He(贺鹏斌)
Chin. Phys. B, 2019, 28 (**1**): 010504. DOI: 10.1088/1674-1056/28/1/010504

Controllable optical superregular breathers in the femtosecond regime

Yang Ren(任杨), Zhan-Ying Yang(杨战营), Chong Liu(刘冲), Wen-Li Yang(杨文力)
Chin. Phys. B, 2018, 27 (**1**): 010504. DOI: 10.1088/1674-1056/27/1/010504

Kuznetsov-Ma soliton and Akhmediev breather of higher-order nonlinear Schrödinger equation

Zai-Dong Li(李再东), Xuan Wu(吴璇), Qiu-Yan Li(李秋艳), P B He(贺鹏斌)
Chin. Phys. B, 2016, 25 (**1**): 010507. DOI: 10.1088/1674-1056/25/1/010507

Parametric instability in the pure-quartic nonlinear Schrödinger equation

Yun-Hong Zhang(张云红)[1,2] and Chong Liu(刘冲)[1,2,3,†]

[1] *School of Physics, Northwest University, Xi'an* 710127, *China*
[2] *Shaanxi Key Laboratory for Theoretical Physics Frontiers, Xi'an* 710127, *China*
[3] *Peng Huanwu Center for Fundamental Theory, Xi'an* 710127, *China*

(Received 20 October 2023; revised manuscript received 28 November 2023; accepted manuscript online 4 December 2023)

We study the nonlinear stage of modulation instability (MI) in the non-intergrable pure-quartic nonlinear Schrödinger equation where the fourth-order dispersion is modulated periodically. Using the three-mode truncation, we reveal the complex recurrence of parametric resonance (PR) breathers, where each recurrence is associated with two oscillation periods (PR period and internal oscillation period). The nonlinear stage of parametric instability admits the maximum energy exchange between the spectrum sidebands and central mode occurring outside the MI gain band.

Keywords: modulation instability, parametric resonance breather, three-mode truncation, energy exchange

PACS: 05.45.–a, 05.10.–a **DOI:** 10.1088/1674-1056/ad11e7

1. Introduction

Modulation instability (MI)[1,2] is a fundamental physical process that exists in a variety of nonlinear systems.[3–6] It is characterized by the dynamical growth and evolution of periodic modulation on a continuous wave background. The MI process can be regarded as a degenerate four-wave mixing process,[7] in which the energy exchange between the central mode (pump) and the spectral sidebands is very intense. This dynamics is closely related to the celebrated Fermi–Pata–Ulam (FPU) recurrence.[8–12] In general, the full evolution of MI in integrable systems can be accurately described by the Akhmediev breathers.[13–17] Performing the Fourier spectral analysis for the Akhmediev breathers, one can obtain an accurate mathematical expression of FPU recurrence.[13,15–17] In contrast, exact description of full evolution of MI in non-integrable systems remains an open issue. It is recently suggested that, the mode truncation method[18–20] can be used to provide an analytical description of the nonlinear stage of MI dynamics in non-integrable systems with parametric resonance (PR).[20–23] It is demonstrated in the periodic nonlinear Schrödinger equation (NLSE) that such parametric instability yields PR breathers in the nonlinear stage, which exhibits periodic oscillation in the evolution direction.[20] These results enrich greatly the types of nonlinear excitations induced by the parametric instability.

In this paper, we consider the parametric instability in the periodic pure-quartic NLSE where the fourth-order dispersion is modulated periodically. It should be pointed out that significant progress has been made on the pure-quartic NLSE in experiments,[24–30] where pure quartic solitons have been observed in photonic crystal waveguides.[24] Such experiments in turn stimulate intense theoretical studies,[31–41] in which nontrivial heteroclinic-structure transition of the pure-quartic MI has been revealed.[35] Thus, we expect more complex properties of parametric instability in the periodic pure-quartic NLSE. By using the Floquet analysis and the three-mode truncation method, we revealed in this paper, the complex nonlinear stage of parametric instability exhibits PR breathers with internal oscillation. These result could be useful for experimental observation of complex PR nonlinear excitations in pure-quartic NLSE optical systems.

2. Physical model and floquet analysis

The periodic pure-quartic NLSE is given by

$$\mathrm{i}\frac{\partial A}{\partial z}+\frac{\beta_4(z)}{24}\frac{\partial^4 A}{\partial t^4}+|A|^2A=0, \tag{1}$$

where z and t are the propagation distance and the retarded time, respectively, and the z-dependent fourth-order dispersion is given by

$$\beta_4(z)=\bar{\beta}_4+\beta_{\mathrm{m}}g_\Lambda(z), \tag{2}$$

where $\bar{\beta}_4$ denotes the average and $g_\Lambda(z)=\cos(k_{\mathrm{g}}z)$ has period $\Lambda=2\pi/k_{\mathrm{g}}$. When the parametric driving is absent, i.e., $\beta_{\mathrm{m}}=0$, equation (1) reduces to pure-quartic NLSE,[24] and the MI exists only when $\bar{\beta}_4<0$. In particular, the nonlinear stage of MI has be achieved recently by the three-mode truncation.[35]

However, in the case when $\beta_{\mathrm{m}}\neq 0$, the MI becomes different. Namely, (i) the MI regime obtained by the Floquet

†Corresponding author. E-mail: chongliu@nwu.edu.cn

© 2024 Chinese Physical Society and IOP Publishing Ltd

analysis switches to $\bar{\beta}_4 > 0$; (ii) the unique nonlinear dynamics of MI should be studied by the method of three-mode truncation.

We start with the Floquet analysis for Eq. (1) which has a continuous wave solution $A_0(z) = \sqrt{P}\mathrm{e}^{\mathrm{i}Pz}$ with $P = |A_0|^2$ being the power. A perturbed solution can be written as $A(z,t) = [p_0(z,t) + \mathrm{i}q_0(z,t) + 1]A_0(z)$ with real functions $p_0(z,t)$ and $q_0(z,t)$ being t-periodic with frequency Ω. Substituting ansatz $A(z,t)$ into Eq. (1) and retaining linear terms, we have

$$\begin{aligned}&\frac{\partial q_0}{\partial z} - \frac{\beta_4(z)}{24}\frac{\partial^4 p_0}{\partial t^4} - 2Pp_0 = 0,\\ &\frac{\partial p_0}{\partial z} + \frac{\beta_4(z)}{24}\frac{\partial^4 q_0}{\partial t^4} = 0.\end{aligned} \tag{3}$$

By using the Fourier transform for the linear system (3) with respect to time t, we have

$$\begin{aligned}&\frac{\partial \hat{q}_0}{\partial z} = \frac{\beta_4(z)}{24}\Omega^4\hat{p}_0 + 2P\hat{p}_0,\\ &\frac{\partial \hat{p}_0}{\partial z} = -\frac{\beta_4(z)}{24}\Omega^4\hat{q}_0.\end{aligned} \tag{4}$$

Our aim is to obtain the Floquet map, which is defined by matrix Φ. The latter satisfies

$$\Phi[\hat{p}_0(0), \hat{q}_0(0)]^{\mathrm{T}} = [\hat{p}_0(\Lambda), \hat{q}_0(\Lambda)]^{\mathrm{T}}.$$

It is given by the fundamental matrix solution of system (4) evaluated at $z = \Lambda$, namely,

$$[\hat{p}_0(n\Lambda), \hat{q}_0(n\Lambda)]^{\mathrm{T}} = \Phi^n[\hat{p}_0(0), \hat{q}_0(0)]^{\mathrm{T}},$$

where n denotes the periods.

We first consider the case when $\beta_{\mathrm{m}} = 0$. From Eq. (4), we have

$$\frac{\partial}{\partial\Lambda}\begin{pmatrix}\hat{p}_0\\ \hat{q}_0\end{pmatrix} = M\begin{pmatrix}\hat{p}_0\\ \hat{q}_0\end{pmatrix}, \tag{5}$$

$$M = \begin{pmatrix}0 & -((\bar{\beta}_4/24)\Omega^4\\ (\bar{\beta}_4/24)\Omega^4 + 2P & 0\end{pmatrix}. \tag{6}$$

By integrating the system (5), the corresponding Floquet map Φ is given by

$$\Phi = \begin{pmatrix}\cos(k\Lambda) & (g\sin(k\Lambda)/k)\\ -h\sin(k\Lambda)/k & \cos(k\Lambda)\end{pmatrix}, \tag{7}$$

where

$$\begin{aligned}&k^2 = gh,\ \ g = -(\bar{\beta}_4/24)\Omega^4,\\ &h = -[(\bar{\beta}_4/24)\Omega^4 + 2P].\end{aligned}$$

In the following discussion, we consider the case $\bar{\beta}_4 = 1$ and $\Lambda = 2\pi/k_g = 1$. The eigenvalues of Eq. (7) is given by

$$\lambda^{\pm} = \mathrm{e}^{\pm\mathrm{i}k\Lambda}. \tag{8}$$

We then consider the case when $\beta_{\mathrm{m}} \neq 0$. Parametric instability occurs when $k(\Omega_p) = p\pi/\Lambda = pk_{\mathrm{g}}/2$ ($p = \pm1, \pm2, \pm3, \ldots$). The latter is the so-called parametric resonance condition. The instability frequency Ω_p correspond to the tips of the Arnold tongues[20]

$$\Omega_p = \sqrt{\sqrt{\frac{24(-P + \sqrt{(p\pi/\Lambda)^2 + P^2})}{\bar{\beta}_4}}}. \tag{9}$$

To do so, we follow the idea proposed in Ref. [20]. Namely, a fiber with periodic dispersion parameters can be thought as two fiber segments a and b with different dispersion parameters. The Floquet map is given by the product of two matrices describing each uniform segment

$$\psi = \Phi_{a\mathrm{v}}\Phi_{b\mathrm{v}}, \tag{10}$$

where $\Phi_{a\mathrm{v}}$ and $\Phi_{b\mathrm{v}}$ are

$$\begin{aligned}\Phi_{a\mathrm{v}} &= \begin{pmatrix}\cos(k_a\Lambda_1) & g_a\sin(k_a\Lambda_1)/k_a\\ -h_a\sin(k_a\Lambda_1)/k_a & \cos(k_a\Lambda_1)\end{pmatrix},\\ \Phi_{b\mathrm{v}} &= \begin{pmatrix}\cos(k_b\Lambda_2) & g_b\sin(k_b\Lambda_2)/k_b\\ -h_b\sin(k_b\Lambda_2)/k_b & \cos(k_b\Lambda_2)\end{pmatrix}.\end{aligned} \tag{11}$$

Here

$$\begin{aligned}&g_a = -\frac{\beta_{4a}}{24}\Omega^4,\ \ h_a = -\left(\frac{\beta_{4a}}{24}\Omega^4 + 2P\right),\\ &g_b = -\frac{\beta_{4b}}{24}\Omega^4,\ \ h_b = -\left(\frac{\beta_{4b}}{24}\Omega^4 + 2P\right).\end{aligned}$$

Here, the eigenvalues of ψ are given by

$$\lambda^{\pm} = \frac{1}{2}\left(2AA_1 - \frac{BB_1g_bk_a}{g_ak_b} - \frac{BB_1g_ak_b}{g_bk_a} \pm \sqrt{\Delta}\right), \tag{12}$$

with

$$\begin{aligned}&\Delta = -4(A^2 + B^2)(A_1^2 + B_1^2)\\ &\quad + \left[-2AA_1 + BB_1\left(\frac{g_bk_a}{g_ak_b} + \frac{g_ak_b}{g_bk_a}\right)\right]^2,\\ &A = \cos(k_a\Lambda_1),\ \ B = \sin(k_a\Lambda_1),\\ &A_1 = \cos(k_b\Lambda_2),\ \ B_1 = \sin(k_b\Lambda_2),\\ &\Lambda_1 = 0.5,\ \ \Lambda_2 = 0.5,\ \ \Lambda = \Lambda_1 + \Lambda_2,\\ &k_a^2 = g_ah_a,\ \ k_b^2 = g_bh_b,\ \ \beta_{4a} = 1 + \beta_{\mathrm{m}},\ \ \beta_{4b} = 1 - \beta_{\mathrm{m}}.\end{aligned}$$

The growth rate, or parametric gain, is represented as

$$G_{\mathrm{F}}(\Omega) = \frac{1}{\Lambda}\ln(\max|\lambda^+|, |\lambda^-|). \tag{13}$$

Figure 1 shows the gain spectra of the periodic pure quartic-NLSE on the (Ω, β_{m}) plane when $\bar{\beta}_4 = 1$. As can be seen, the Floquet analysis shows the MI bands which are presently known as Arnold tongues[20,22] [Fig. 1(a)]. Such the MI exhibits narrow band around the tongue tip frequencies Ω_p.

Moreover, the profiles of the gain spectra when $\beta_{\rm m}=2$ shown in Fig. 1(b). Clearly, different Ω_p are generally incommensurate, which greatly reduces the possibility that the harmonics of a probed frequency experience exponential amplification due to higher-order bands. Thus, the nonlinear stage of such MI can be studied by the method of three-modes truncation.

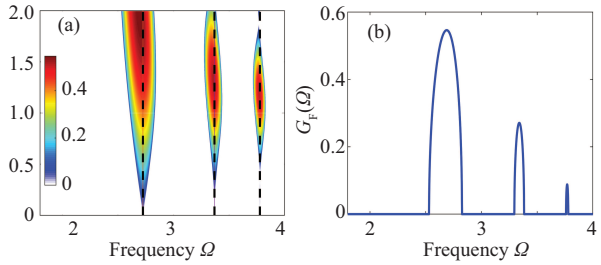


Fig. 1. Results of the linear Floquet analysis for Eq. (1). (a) False color plot showing the first three Arnold tongues in the plane $(\Omega,\beta_{\rm m})$. The black dotted line represents the Ω_p, $p=1,2,3$. (b) The gain curve $G_{\rm F}(\Omega)$ at $\beta_{\rm m}=2$. In this paper, we focus on the wave dynamics in the first PR band.

3. The three-mode truncation method

Three-mode model allows us to unveil the nonlinear stage of parametric instability for the periodic pure-quartic NLSE. We consider the harmonically perturbed plane wave (HPPW) as follows:

$$A(z,t)=A_0(z)+\frac{A_1(z)}{\sqrt{2}}(\mathrm{e}^{-\mathrm{i}\Omega t}+\mathrm{e}^{\mathrm{i}\Omega t}). \tag{14}$$

Substituting it into Eq. (1) and leaving only these three terms: $\mathrm{e}^{-\mathrm{i}\Omega t}$, e^{0}, $\mathrm{e}^{\mathrm{i}\Omega t}$, we have

$$\begin{aligned}-\mathrm{i}\frac{\partial A_0}{\partial z}&=(|A_0|^2+2|A_1|^2)A_0+A_1^2A_0^*,\\ -\mathrm{i}\frac{\partial A_1}{\partial z}&=\left(\frac{\beta_4(z)\Omega^4}{24}+2|A_0|^2+\frac{3|A_1|^2}{2}\right)A_1+A_0^2A_1^*.\end{aligned} \tag{15}$$

Generally, $|A_1|^2+|A_0|^2=P=1$ is conserved quantity. Equation (15) can be cast in the Hamiltonian form

$$\dot{\eta}=-\frac{\partial H}{\partial\Delta\phi},\quad \Delta\dot{\phi}=\frac{\partial H}{\partial\eta}, \tag{16}$$

where

$$\begin{aligned}H=&-\frac{3\eta^2}{4}+\frac{\kappa}{2}\eta+|C_p|\,\eta(1-\eta)\cos2\Delta\phi\\&-\alpha\eta(1-3\eta+2\eta^2),\end{aligned} \tag{17}$$

where $\eta\approx|A_1|^2$, $\Delta\phi=\phi_1(z)-\phi_0(z)+\phi_p/2$ in which, $\phi_1(z)\approx{\rm Arg}[A_1(z)]$, $\phi_0(z)\approx{\rm Arg}[A_0(z)]$, $\phi_p={\rm Arg}[C_p]$, $\Delta\phi$ is overall phase, $C_n=(-1)^nJ_n(\beta_{\rm m}\Omega^4/(12k_{\rm g}))$, only the primary sideband of parametric resonances is considered, that is to say $p=1$, $C_0=J_0(\beta_{\rm m}\Omega^4/(12k_{\rm g}))$, $C_1=-J_1(\beta_{\rm m}\Omega^4/(12k_{\rm g}))$, hence $\phi_p={\rm Arg}[C_1]=\pi$, $\alpha(\Omega)\approx(1/k_{\rm g})[(|C_0|^2+|C_1|^2)/2]$. A crucial parameter $\kappa\equiv\bar{\beta}_4\Omega^4/12-pk_{\rm g}+2P$, when $\kappa=0$, $\bar{\beta}_4\Omega^4/12+2P=pk_{\rm g}$, this value corresponds to the quasi-phase matching relation of the parametric resonance.

For the periodic pure-quartic NLSE, H exists four groups of stationary points $(\Delta\phi_{\rm e},\eta_{\rm e})$ (the solution of $\dot{\eta}=\Delta\dot{\phi}=0$). Namely,

$$\begin{aligned}(\Delta\phi_{\rm e},\eta_{\rm e})&=\left(\pm\frac{1}{2}\arccos\left[\frac{2\alpha-\kappa}{2|C_p|}\right],0\right),\\(\Delta\phi_{\rm e},\eta_{\rm e})&=\left(\pm\frac{1}{2}\arccos\left[\frac{-3-2\alpha+\kappa}{2|C_p|}\right],1\right),\\(\Delta\phi_{\rm e},\eta_{\rm e})&=\left(0\text{ or }\pi,\frac{-3-4|C_p|+12\alpha-\sqrt{\Theta}}{24\alpha}\right),\\(\Delta\phi_{\rm e},\eta_{\rm e})&=\left(\frac{\pi}{2}\text{ or }-\frac{\pi}{2},\frac{-3+4|C_p|+12\alpha-\sqrt{\Theta}}{24\alpha}\right),\end{aligned} \tag{18}$$

where

$$\Theta=9+24|C_p|+16|C_p|^2-72\alpha+48\alpha^2+48\alpha\kappa.$$

Figure 2 shows the bifurcation diagram and the level set of H versus frequency Ω. Firstly, in the frequency range of Arnold tongue, the heteroclinic separatrix ($\eta_{\rm e}=0$) divides the phase plane into inner and outer orbits [see Fig. 2(b)]. Secondly, once the frequency fall outside the Arnold tongue, the topological structure of Hamiltonian H will suddenly change, and the new heteroclinic separatrix divides the phase plane into three different domains [see Figs. 2(c) and 2(d)]. On the bifurcation diagram [see Fig. 2(a)], the red and green lines intersect. It is worth noting that by comparing Figs. 2(c) and 2(d), the heteroclinic separatrix will change to $\eta_{\rm e}=1$ from $\eta_{\rm e}=0$ at the intersection of the two lines.

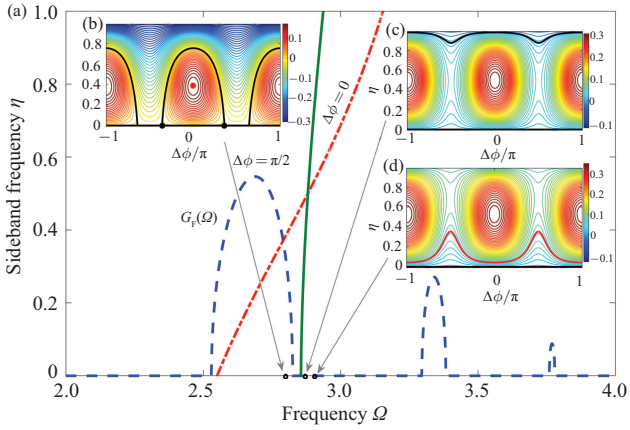


Fig. 2. Bifurcation diagram and the level set of H. (a) Normalized sideband fraction η for the nonlinear eigenmodes as a function of normalized frequency Ω; the red lines correspond to $\Delta\phi=0$, stable; the green lines corresponding to $\Delta\phi=\pi/2$, unstable; the blue lines is the gain $G_{\rm F}(\Omega)$ when $\beta_{\rm m}=2$. Panels (b) and (d) show the Hamiltonian contours when $\Omega=2.8$ inside PR gain bandwidth and $\Omega=2.87$, $\Omega=2.9$, beyond the PR gain bandwidth, respectively.

To get a deeper understanding of the dynamics, we analyzed the stability of the eigenmodes. It is checked by the given perturbation solution $(\Delta\phi,\eta)=(\Delta\phi_{\rm e}+\delta\phi,\eta_{\rm e}+\delta\eta)$.

After linearizing the eigenmodes, the Jacobian matrix is given by

$$J=\begin{pmatrix} 2|C_p|(1-2\eta_e)\chi_1 & 4|C_p|\eta_e(1-\eta_e)\chi_2 \\ 6\alpha-12\alpha\eta_e-3/2-2|C_p|\chi_2 & -2|C_p|(1-2\eta_e)\chi_1 \end{pmatrix}, \tag{19}$$

where $\chi_1=\sin 2\Delta\phi_e$, $\chi_2=\cos 2\Delta\phi_e$, and the eigenvalues of the Jacobian matrix are denoted as

$$\lambda^{\pm}=\pm\sqrt{2|C_p|[\eta_e\chi_2 N+2|C_p|\chi_1(1-4\eta_e+4\eta_e^2)]}, \tag{20}$$

where

$$N=-3+12\alpha+3\eta_e-36\alpha\eta_e+24\alpha\eta_e^2 +4|C_p|\chi_2(\eta_e-1).$$

For the first two sets of eigenmodes, $\eta_e=0$ and $\eta_e=1$, the eigenvalues $\lambda^{\pm}=\pm 2|C_p\sin 2\Delta\phi_e|$ are real and they have opposite signs. The two sets of eigenmodes are represented as saddle points [the black dots in Fig. 2(b)] on the level set of the phase plane, which can represent the combination of instability and stability of the nonlinear orbits in different directions. In other words, it can evolve towards both an internal orbit and an external orbits. For the third set of the eigenmodes, $\Delta\phi_e=0$, the eigenvalues $\lambda^{\pm}$ are pure imaginary which represents a stable center point (the red dots in Fig. 2(b)). All the nonlinear orbits in its vicinity will rotate in a closed form. Especially if the disturbance is small enough, and the corresponding homoclinic orbits will shrink the stable center point. For the fourth set of the eigenmodes, $\Delta\phi_e=\pi/2$, the eigenvalues $\lambda^{\pm}$ are real, which correspond to the saddle points of the Hamiltonian H.

4. Heteroclinic structures

The structure illustrated in Fig. 2 can characterize the nonlinear stage of parametric instability of the pure-quartic NLSE. To illustrate this point, we numerically integrate Eq. (1). The initial input condition is given by

$$A_0(0,t)=\sqrt{1-\eta_0}+\sqrt{2\eta_0}\,e^{i\theta_0}\cos(\Omega t), \tag{21}$$

where $\eta_0\ll 1$, and $\Delta\phi_0=\theta_0+\phi_p/2$.

Our discussion begins with the near-separation line dynamics of the system. As shown in Figs. 3(a) and 3(b), nonlinear excitations induced by the PR are observed. Such nonlinear excitations are the PR breathers. The spectra exhibit FPU-like recurrence [see Figs. 3(c) and 3(d)]. We found that the nonlinear pattern with initial phase $\Delta\phi_0=\pi/2$ is similar to that with the phase $\Delta\phi_0=0$. However, such the two patterns correspond to different phase trajectories [see Figs. 3(e) and 3(f)]. When $\Delta\phi_0=0$, the trajectory is inside the separatrix, and the whole trajectory rotates to become a homoclinic cycles [see Fig. 3(e)]. When $\Delta\phi_0=\pi/2$, the trajectory spans the entire phase plane $(-\pi,\pi)$ [see Fig. 3(f)]. Due to the rapid oscillations in the evolutionary direction, the effect of the initial phase on the evolution pattern cannot be directly revealed from the space–time evolution. This is an important characteristic of the hidden heteroclinic structure of PR in the periodic NLSE. By comparing to the numerical results of Eq. (16) (the red curve) with Eq. (1) (the blue scatter curve), there is a slight deviation between the numerical results of Eqs. (16) and (1), This is due to the fact that the three-mode truncation ignores the higher-order sidebands.

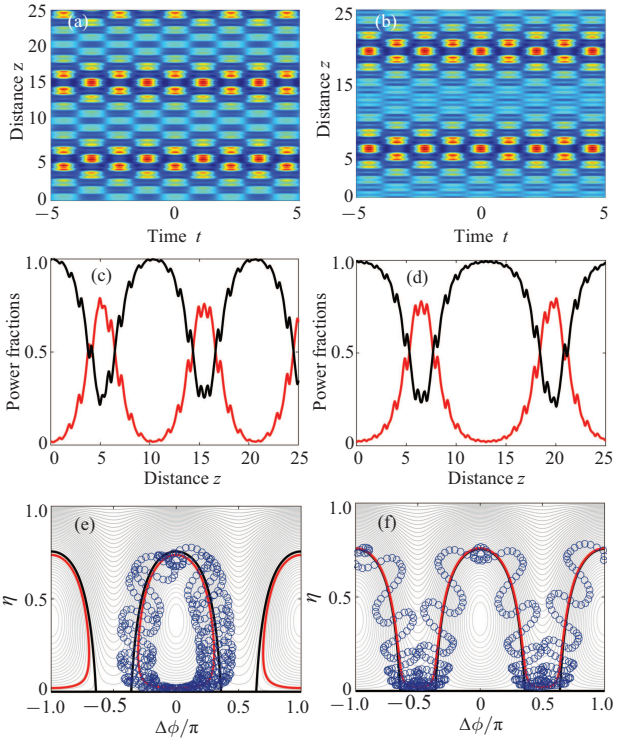


Fig. 3. Two types of quasiperiodic recurrences from numerical integration of Eq. (1). (a) The intensity $|A|^2$ when $\Delta\phi_0=0$. (b) The intensity $|A|^2$ when $\Delta\phi_0=\pi/2$. (c), (d) Fourier modes of central pump $|A_0|^2$ (black lines) and sideband power $|A_1|^2$ (red lines) versus z when $\Delta\phi_0=0$ and $\Delta\phi_0=\pi/2$, respectively. (e), (f) Projections of the quasiperiodic recurrences in phase plane with $\Delta\phi_0=0$ and $\Delta\phi_0=\pi/2$, respectively. Here $\beta_m=2$, $\eta_0=0.02$, and $\Omega=2.8$.

When $\eta=0.001$, $\Delta\phi_0=0.298639\pi$, the heteroclinic separatrix in the phase plane is obtained. The nonlinear evolution is shown in Fig. 4(a).

Another interesting result is the internal oscillation structure of the PR breathers as shown in Fig. 4(b). To illustrate clearly this point, we extract the evolution of the separatrix with different β_m. Moreover, by defining the parametric resonance period D_1 (the distance between the two peaks formed by the parameter resonance) and the internal oscillation period D_2 (the number of internal oscillation peaks contained in one

resonance period), we analyzed the variation of the two periods in Fig. 4(d) versus $\beta_{\rm m}$. As can be seen from the figure, D_1 keeps unchanged once the modulation frequency $k_{\rm g}$ is fixed. However, D_2 varies as $\beta_{\rm m}$ increases. Specifically, with $\beta_{\rm m}$ increasing from 0, the oscillating structure began to appear inside the parametric resonance. Then, D_2 gradually decreases. When $\beta_{\rm m}=0.9$, the internal oscillation period reaches saturation. As $\beta_{\rm m}=2.6$, D_2 increases again, and the internal oscillation decreases.

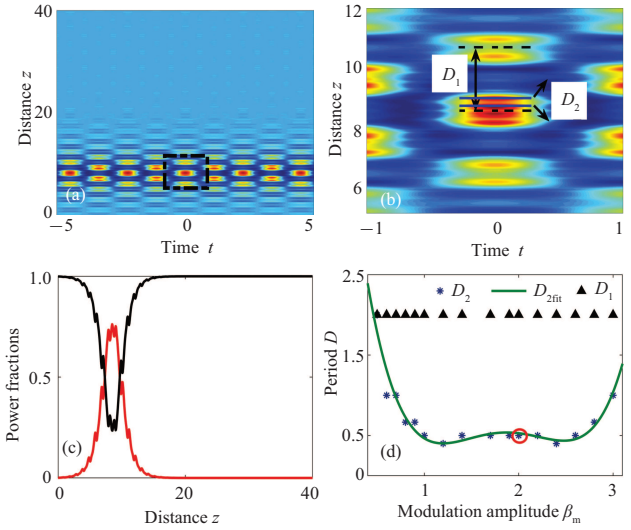


Fig. 4. The evolution of PR breathers through numerical integration of Eq. (1). (a) The PR breathers of the intensity $|A|^2$ correspond to the separatrix. Here $\beta_{\rm m}=2$, $\Omega=2.8$, $\eta_0=0.001$, and the initial phase $\Delta\phi_0=0.298639\pi$. (b) Enlarged view of the structure of the region inside the dotted line in panel (a). (c) Fourier modes of the central pump $|A_0|^2$ and the first-order sidebands $|A_1|^2$ *versus* z. (d) The variation of two periods D_1 and D_2 with $\beta_{\rm m}$. The red circle corresponds to D_2 in panel (b).

5. The energy exchange between spectrum sidebands and the pump

Linear stability analysis suggests that the sideband growth rate is the largest at the frequency corresponding to the maximum gain $G_{\rm F}$, i.e., the conversion efficiency of the central pump and sideband is the largest. However, as shown in Fig. 2(a), the intersection of the two lines on the bifurcation diagram falls outside the Arnold tongue. Thus, we guess that the strongest nonlinear transition occurs at frequencies outside the PR bandwidth.

Figure 5(a) shows the variation of the maximum achievable sideband as a function of frequency. It can be seen that the sideband fraction almost increases until it reaches the maximum at the frequency $\Omega_{\rm c}$. Beyond the critical frequency $\Omega_{\rm c}$, the energy contained in the sideband becomes lower, proving that the transition suddenly drops. Obviously, the result of nonlinear analysis deviates from that of Floquet (linear) analysis. There is a strong contrast between the frequency conversion dynamics before and after the frequency $\Omega_{\rm c}$ [see Figs. 5(b) and 5(c)]. Their evolutionary trajectories are located in different regions of the phase plane [Figs. 5(d) and 5(e)]. The critical frequency corresponding to the evolution along the heteroclinic orbit in Fig. 2(c) can be calculated as the implicit solution of equation

$$\begin{aligned} &H(\Delta\phi=0,\ \eta(\Omega))=H(\Delta\phi_0,\eta_0),\ \ \Omega\le\Omega_{\rm c},\\ &H(\Delta\phi=\pm\frac{\pi}{2},\ \eta(\Omega))=H(\Delta\phi_0,\eta_0),\ \ \Omega>\Omega_{\rm c}. \end{aligned}\tag{22}$$

This indicates that the largest achievable sideband occurs at $\Omega=\Omega_{\rm c}$.

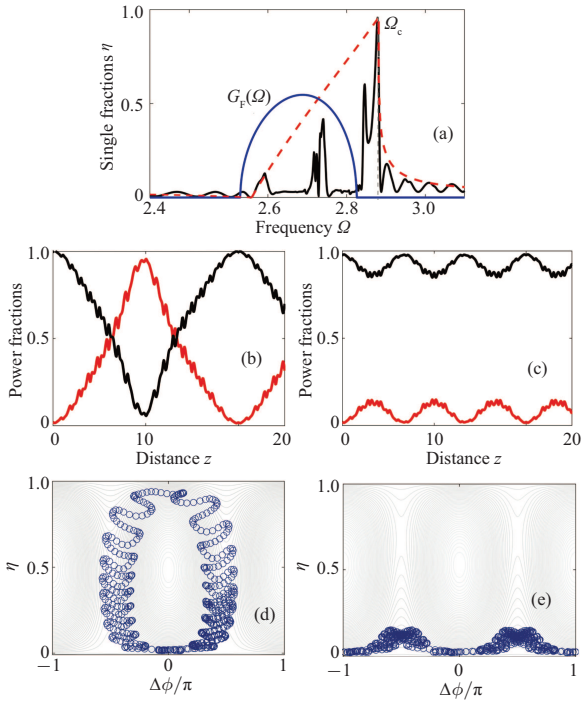


Fig. 5. (a) The output sideband fraction $\eta(z=10)$ versus Ω from numerical integration for $\eta_0=0.03$ and $\Delta\phi_0=0$ (solid black curve); the red curve gives the maximum achievable conversion from Eq. (22), with superimposed small-signal PR gain $G_{\rm F}$ (blue curve). (b), (c) Pump and sideband mode evolutions with the same initial condition around $\Omega_{\rm c}$, they are $\Omega=2.87$ and $\Omega=2.9$, respectively. (d), (e) Corresponding evolution trajectories of panels (b) and (c) on the phase plane. Here $\beta_{\rm m}=2$, $\eta_0=0.02$, and the initial phase $\Delta\phi_0=0$.

6. Conclusion

In conclusion, we study the parametric instability in the periodic pure-quartic NLSE by using the Floquet analysis and the three-mode truncation method. We obtain the PR breathers with internal oscillation. Within the frequency range of Arnold tongue, the phase plane is divided into internal and external orbits by the heteroclinic separatrix. Once the modulation frequency exceeds the MI range, the heteroclinic separatrix will separate the phase plane into three different regions.

Moreover, we demonstrated that the maximum energy exchange between the spectrum sidebands and pump occurs outside the gain bandwidth. Our results reveal the richness of nonlinear dynamics in periodic pure-quartic NLSE, which

could be useful for experimental observation of complex PR nonlinear excitations in pure-quartic NLSE optical systems.

Acknowledgements

Project supported by the National Natural Science Foundation of China (Grant Nos. 12175178 and 12247103), the Natural Science Basic Research Program of Shaanxi Province, China (Grant No. 2022KJXX-71), and the Shaanxi Fundamental Science Research Project for Mathematics and Physics (Grant No. 22JSY016).

References

[1] Benjamin T B and Feir J 1967 *J. Fluid Mech.* **27** 417
[2] Zakharov V and Ostrovsky L 2009 *Physica D* **238** 540
[3] Whitham G B 1965 *Physical and Engineering Sciences* **283** 238
[4] Taniuti T and Washimi H 1968 *Phys. Rev. Lett.* **21** 209
[5] Abdullaev F Kh, Baizakov B B, Darmanyan S A, Konotop V V and Salerno M 2001 *Phys. Rev. A* **64** 043606
[6] Andrade D and Stuhlmeier R 2023 *J. Fluid Mech.* **958** 1103
[7] Cappellini G and Trillo S 1991 *J. Opt. Soc. Am.* **8** 824
[8] Lake B M, Yuen H C, Rungaldier H and Ferguson W E 1977 *J. Fluid Mech.* **83** 49
[9] Simaeys G V, Emplit P and Haelterman M 2001 *Phys. Rev. Lett.* **87** 033902.
[10] Akhmediev N 2007 *Nature* **413** 267
[11] Kimmoun O, Hsu H C, Branger H, Li M S, Chen Y Y, Kharif C, Onorato M, Kelleher E J R, Kibler B, Akhmediev N and Chabchoub A 2016 *Sci. Rep.* **6** 28516
[12] Pierangeli D, Flammini M, Zhang L, Marcucci G, Agranat A J, Grinevich P G, Santini P M, Conti C and DelRe E 2018 *Phys. Rev. X* **8** 041017
[13] Akhmediev N and Korneev V 1986 *Theoret. Math. Phys.* **69** 1089
[14] Dudley J M, Genty G, Dias F, Kibler B and Akhmediev N 2009 *Opt. Express* **24** 21497
[15] Liu C, Wu Y H, Chen S C, Yao X K and Akhmediev N 2021 *Phys. Rev. Lett.* **127** 094102
[16] Chen S C, Liu C, Yao X K, Zhao L C and Akhmediev N 2021 *Phys. Rev. E* **104** 024215
[17] Chen S C and Liu C 2022 *Physica D* **438** 133364
[18] Trillo S and Wabnitz S 1991 *Opt. Lett.* **16** 986
[19] Mussot A, Naveau C, Conforti M, Kudlinski A, Copie F, Szriftgiser P and Trillo S 2018 *Nat. Photon.* **12** 303
[20] Conforti M, Mussot A, Kudlinski A, Rota Nodari S, Dujardin G, De Biévre S, Armaroli A and Trillo S 2016 *Phys. Rev. Lett.* **117** 013901
[21] Zhu C X, Yi W, Guo G C and Zhou Z W 2019 *Phys. Rev. A* **99** 023619
[22] Conforti M, Copie F, Mussot A, Kudlinski A and Trillo S 2016 *Opt. Lett.* **41** 5027
[23] Staliunas K, Hang C and Konotop V V 2013 *Phys. Rev. A* **88** 023846
[24] Blanco-Redondo A, de Sterke C M, Sipe J E, Krauss T F, Eggleton B J and Husko C 2016 *Nat. Commun.* **7** 10427
[25] Blanco-Redondo A, de Sterke C M , Husko C and Eggleton B 2017 *Opt. Lett.* **47** 3800
[26] Lo C W, Stefani A, de Sterke C M and Blanco-Redondo A 2018 *Opt. Express* **26** 7786
[27] Taheri H and Matsko A B 2019 *Opt. Lett.* **44** 3086
[28] Zhang Z X, Luo M, Chen J X, Chen L H, Liu M, Luo A P, Xu W C and Luo Z C 2022 *Opt. Lett.* **47** 1750
[29] Qian Z C, Liu M, Luo A P, Luo Z C and Xu W C 2022 *Opt. Express* **30** 22066
[30] Runge F A, Hudson D D, Tam K K K, de Sterke C M and Blanco-Redondo A 2020 *Nat. Photon.* **14** 492
[31] Zeng J L, Dai J X, Hu W and Lu D Q 2022 *Appl. Math. Lett.* **129** 107923
[32] Tam K K K, Alexander T J, Blanco-Redondo A and de Sterke C M 2019 *Opt. Lett.* **44** 3306
[33] Zhao K, Gao C, Xiao X and Yang C 2021 *Opt. Lett.* **46** 761
[34] de Sterke C M, Runge A F J, Hudson D D and Blanco-Redondo A 2021 *APL Photon.* **6** 091101
[35] Yao X K, Liu C, Yang Z Y and Yang W L 2022 *Phys. Rev. Res.* **4** 013246
[36] Tabi C B, Tagwo H, Tiofack C G L and Kofané T C 2022 *Opt. Lett.* **47** 5557
[37] Li Y H, Dai J X, Liu J S, Weng Z W, Hu W and Lu D Q, 2022 *Opt. Commun.* **524** 128790
[38] Wang Z T, Luo C Y, Wang Y W, Ling X H and Zhang L F 2022 *Opt. Lett.* **47** 3800
[39] Dai J X, Zeng J L, Hu W and Lu D Q 2022 *Chaos, Solitons and Fractals* **165** 112867
[40] Zhu Z W, Yang S, He C J and Lin X C 2023 *Chaos, Solitons and Fractals* **175** 113978
[41] Tiofack C G L , Tabi C B, Tagwo H and Kofané T C 2023 *Phys. Lett. A* **480** 128982